PHYSICAL REVIEW B **109**, 054308 (2024)

Editors' Suggestion

Bloch-wave interferometry of driven quasiparticles in bulk GaAs

Seamus D. O'Hara,[1,2,*] Joseph B. Costello,[1,2] Qile Wu,[1,2] Ken West,[3] Loren Pfeiffer,[3] and Mark S. Sherwin[1,2,†]
[1] *Physics Department, University of California, Santa Barbara, California 93106, USA*
[2] *Institute for Terahertz Science and Technology, University of California, Santa Barbara, California 93106, USA*
[3] *Electrical Engineering Department, Princeton University, Princeton, New Jersey 08544, USA*

(Received 19 May 2023; revised 22 January 2024; accepted 24 January 2024; published 20 February 2024)

We show that the polarizations of sidebands emitted from bulk gallium arsenide driven by a strong terahertz (THz) field while probed with a weak near-infrared laser can be viewed as interferograms from a Michelson-like interferometer for Bloch waves. The fringe contrast of an interferogram is a measure of the nonequilibrium dephasing of Bloch waves in this strongly driven system. An interferogram's oscillation frequency is determined by, among other factors, the THz field strength F_{THz} and the reduced masses of electron-hole pairs. A simple analytic model brings all measured and calculated spectra into agreement with adjustment of only a single dephasing constant, and predicts the scaling of interferograms with F_{THz}.

DOI: 10.1103/PhysRevB.109.054308

I. INTRODUCTION

Since Thomas Young demonstrated the wave nature of light through interference phenomena, physicists have invented many kinds of interferometers to extract information from the differences in phase between superimposed waves. For example, A. A. Michelson invented the interferometer that bears his name to reject the hypothesis of a stationary luminiferous ether [1]. After the advent of quantum mechanics, Thomson and Davisson used interference phenomena to demonstrate the wave nature of free electrons [2,3]. Decades later, a Young's-type double-slit experiment demonstrated the wave nature of cold atoms [4]. The dynamic phase of a matter wave is sensitive to its acceleration, which has been exploited to measure inertial forces by interfering atoms evolving over two quantum paths in, for example, a Mach-Zehnder interferometer configuration [5].

Near thermal equilibrium, measurements in solids have yielded observations of interference phenomena such as standing electronic Bloch waves on metal surfaces [6–8]. Furthermore, both electronic Young's double-slit interferometers [9] and Mach-Zehnder-type interferometers [10] have been realized in quasi-2D electron gases in gallium arsenide (GaAs). However, in these near-equilibrium systems the electrons do not accelerate, and thus the inertial properties of quasiparticles, which can be represented as packets of Bloch waves, cannot be directly probed.

Charged quasiparticles accelerated by electric fields scatter rapidly, complicating the observation of interference phenomena far from equilibrium. The recent development of strong laser fields addresses this problem by enabling coherent acceleration of quasiparticles on picosecond and sub-picosecond time scales [11,12]. In high-harmonic generation (HHG) in solids, a single strong laser field creates and then accelerates charged excitations [13–18]. HHG enables studies of quasiparticle dynamics with attosecond resolution [19,20], and is sensitive to many details of the interactions of quasiparticles with their host crystals [19–24]. In 2015, time-resolved interferences of quasiparticles were observed in HHG in a semiconductor driven by strong terahertz pulses [18]. However, such quantum interferences in HHG cannot be easily attributed to a small number of momentum-space trajectories for the Bloch waves. A Huygens-Fresnel picture of HHG has been recently proposed [25], in which each Bloch wave created by the laser field is treated as a composition of an infinite number of wavelets, and the HHG spectrum is calculated by integrating over the interfering contributions from all wavelets. This picture does not map onto a familiar interferometer, and thus it is not yet simple to extract information about the inertial properties of quasiparticles from an HHG spectrum.

In this paper, we demonstrate that a related process, high-order sideband generation (HSG) [26–32], can be viewed as the output of a Michelson interferometer for Bloch waves associated with electron-hole pairs. In HSG, two lasers with different frequencies are used. A relatively weak laser tuned near the band gap of a semiconductor—bulk GaAs for the experiments presented here—creates electron-hole pairs, and a second, stronger, lower-frequency laser accelerates them to higher energy. The use of two frequencies separates the contributions of intraband excitations and interband dynamics to the final HSG signal [33]. The Bloch-wave interferograms are sideband polarizations as functions of sideband photon energy. We show that these Bloch-wave interferograms can be calculated by using a simple analytic model whose only inputs are (a) the THz field strength F_{THz} and frequency and (b) inertial properties of the electrons and holes, namely their effective masses along the direction of the THz field, and a single nonequilibrium dephasing rate. The latter determines the fringe contrast of the observed interferograms. Using a

---

[*] seamuso@sas.upenn.edu
[†] sherwin@physics.ucsb.edu

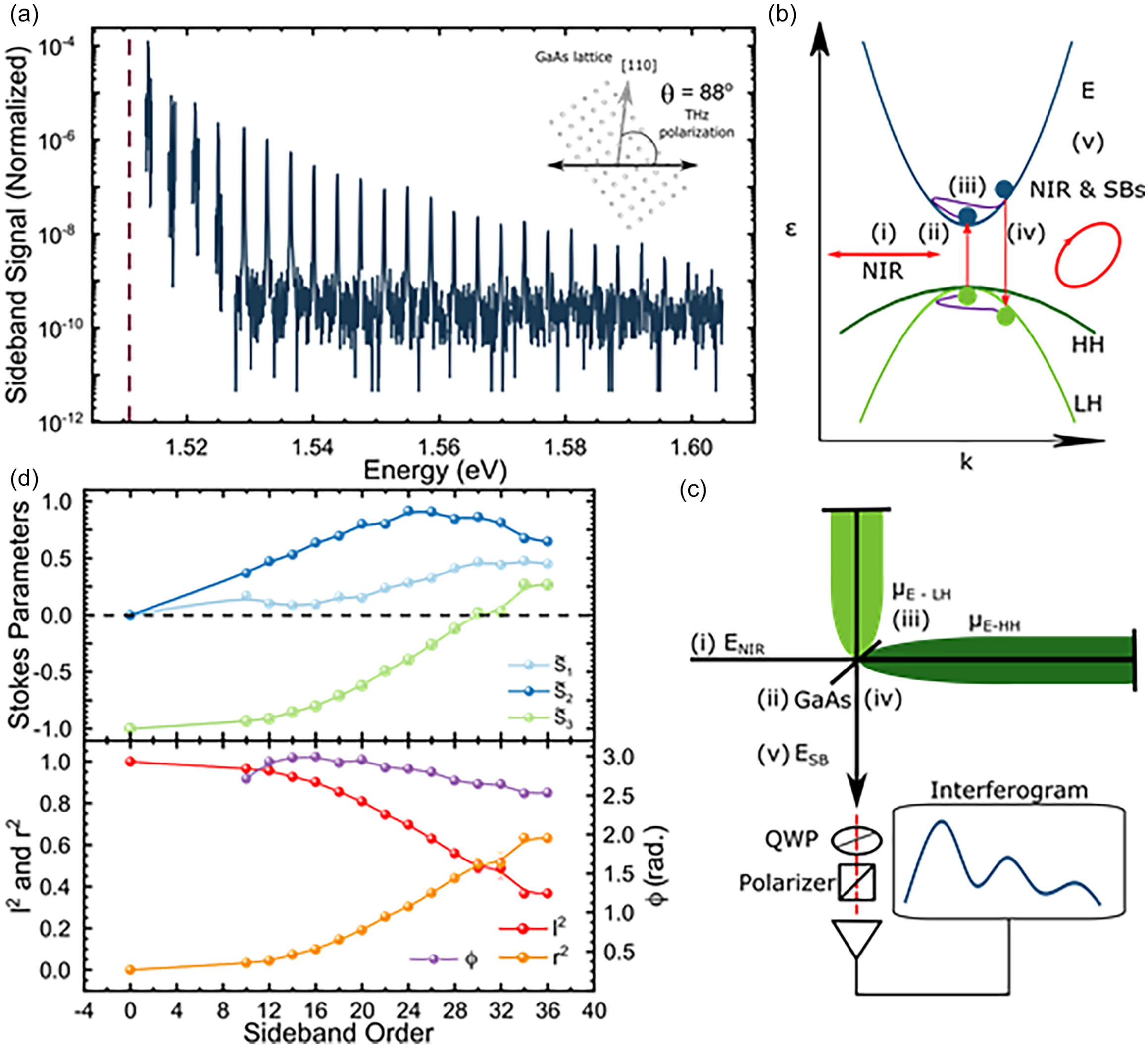

FIG. 1. Description of high-order sideband generation (HSG) in bulk GaAs as a Michelson interferometer for Bloch waves. (a) An example of a sideband spectrum taken at THz field strength $F_{\mathrm{THz}} = 70$ kV/cm with NIR laser frequency at red dashed line. (Inset) The crystal orientation of the GaAs crystal with respect to the THz field. (b) A representation of HSG in momentum space showing electron (E), heavy-hole (HH), and light-hole (LH) bands. (c) A Michelson interferometer for Bloch waves. The Roman numerals in (b) and (c) label the following processes. (i) A NIR laser is incident on the bulk GaAs. (ii) The bulk GaAs acts like a beam-splitter, converting the NIR laser beam into E-HH and E-LH pairs. (iii) In the two interferometer arms, Bloch waves of E-HH and E-LH pairs propagate along different k-space trajectories and acquire different phases. (iv) These Bloch waves merge at the beam-splitter and (v) sidebands are emitted. Bloch-wave interferograms of sideband polarizations are recorded by Stokes polarimetry with a quarter-wave plate (QWP) and a polarizer. (d) Stokes polarimetry and a Bloch-wave interferogram. (Top) Three normalized Stokes parameters $\tilde{S}_1$, $\tilde{S}_2$, and $\tilde{S}_3$ corresponding to the sideband spectrum in (a). (Bottom) a Bloch-wave interferogram that is the sideband polarization as a function of sideband order n. The polarization of the nth-order sideband is represented as a normalized state in the basis of circular polarizations, $|E_{\mathrm{SB},n}\rangle = l(n)e^{i\phi(n)}|L\rangle + r(n)|R\rangle$, where $l(n)$, $r(n)$, and $\phi(n)$ are real functions of n (see Appendix C 2 for definitions of the basis states).

scaling relation predicted by our model, we show that Bloch-wave interferograms recorded with different F_{THz} collapse onto a single curve.

II. EXPERIMENT: HIGH-ORDER SIDEBAND GENERATION

An example spectrum of high-order sideband generation (HSG) is displayed in Fig. 1(a). Each peak represents a sideband with a photon energy $\hbar\Omega_{\mathrm{NIR}} + n\hbar\omega$, where $\hbar\Omega_{\mathrm{NIR}}$ and $\hbar\omega$ are respectively the photon energies of the near-infrared (NIR) and terahertz (THz) lasers, and the sideband order n is an even integer. Sidebands were generated from a 500-nm-thick bulk gallium arsenide (GaAs) epilayer grown via molecular beam epitaxy. We tune the NIR laser close to the estimated bandgap of the GaAs sample at 35 K with a wavelength of 820.6 nm (see Appendix A for a discussion). The THz field has a frequency $f_{\mathrm{THz}} = 447 \pm 1$ GHz [31] and a pulse duration of 40 ns.

The GaAs epilayer came from the same GaAs wafer used in Ref. [34] and the sample was prepared in the same way as described in Ref. [34]. One goal of the sample fabrication was to make sure that the GaAs epilayer was uniformly and minimally strained. Another goal was to make the sample transmissive to sidebands in the NIR spectral range while maximizing the THz field strength at the GaAs epilayer (see Appendix B for a discussion of the THz field strength). To provide mechanical support while allowing the transmission of NIR sidebands, following the method described in Refs. [35–38], we transferred the GaAs epilayer to a clean 488 μm thick c-axis grown sapphire wafer, which was chosen because its in-plane thermal expansion coefficient is close to that of GaAs. In order to enhance the THz field strength at the GaAs epilayer, an indium tin oxide (ITO) layer was deposited onto the back of the sapphire to create a cavity by using electron-beam deposition, as detailed in Ref. [34]. Before the HSG experiment, the sample was mounted in the cryostat, attached to the cold finger with a thermally conductive and vacuum-safe adhesive, and cooled down to 35 K. Cooling down to cryogenic temperatures can induce some strain in the GaAs epilayer. The NIR laser was focused on a sample spot over which the small strain is uniform (see Appendix A for a discussion).

III. MICHELSON INTERFEROMETER FOR BLOCH WAVES

Like HHG, HSG is summarized in three steps [26], displayed in a momentum-space, semiclassical picture in Fig. 1(b). First, a NIR laser creates an electron-hole pair, where the hole is in a superposition of heavy-hole (HH) and light-hole (LH) states. Second, a linearly-polarized THz field drives the electron-hole (E-H) pairs towards higher quasimomenta. Third, the electron and hole recombine to generate a sideband photon. The microscopic processes of HSG in GaAs described in Fig. 1(b) have been labeled i to v to map them onto different components of a Michelson interferometer for Bloch waves, shown in Fig. 1(c). The NIR laser is incident on the bulk GaAs (i), which acts like a beam splitter (ii), creating E-H states in one or both arms. Under the THz field, the E-HH and E-LH Bloch waves propagate along different k-space trajectories (iii). Because the E-HH and E-LH reduced masses determine the dispersion relations for Bloch waves, they are analogous to refractive indices that determine the dispersion relations for light waves in the arms of a conventional Michelson interferometer. In the Michelson interferometer for Bloch waves, the effective arm lengths, which determine the quantum mechanical phases acquired by E-HH and E-LH pairs, increase with increasing sideband order for a fixed THz field. Upon sideband emission, the E-HH and E-LH Bloch waves merge at the beam splitter (iv), coupling out of the interferometer. Bloch-wave interferograms of the outgoing sideband electric field (v) consist of the sideband polarizations as functions of sideband order.

We record our Bloch-wave interferograms using Stokes polarimetry, where all four Stokes parameters for each sideband are measured (see Appendix C 1 for details). The top frame of Fig. 1(d) shows three Stokes parameters, S_1, S_2, and S_3 normalized as $\tilde{S}_j = S_j/\sqrt{S_1^2 + S_2^2 + S_3^2}$ ($j = 1, 2, 3$). The corresponding Bloch-wave interferograms are shown in the bottom frame, where the data points for $n = 0$ represent the polarization of the NIR laser. The polarization of the nth-order sideband is represented as a normalized state in the basis of circular polarizations, $|E_{\mathrm{SB},n}\rangle = l(n)e^{i\phi(n)}|L\rangle + r(n)|R\rangle$. The functions $l(n)$, $r(n)$, and $\phi(n)$ are real and satisfy

$$\phi(n) = \tan^{-1}\left(\frac{\tilde{S}_2(n)}{\tilde{S}_1(n)}\right) - 2\theta - \frac{\pi}{2}, \tag{1}$$

$$l^2(n) = \frac{1 - \tilde{S}_3(n)}{2} = 1 - r^2(n), \tag{2}$$

where θ is the angle between the crystal axis [110] and the linear polarization of the THz field. The angle θ was measured as 88° [inset of Fig. 1(a)].The left- and right-handed circularly polarized states, $|L\rangle$ and $|R\rangle$, are defined with respect to the crystal axes of bulk GaAs [see Appendix C 2 for the details].

Following Ref. [34], the relation between the electric fields of the nth-order sideband and the NIR laser, $\mathbf{E}_{\mathrm{SB},n}$ and $\mathbf{E}_{\mathrm{NIR}}$, can be written as

$$\mathbf{E}_{\mathrm{SB},n} \propto \sum_{s=1,2} \begin{pmatrix} \mathbf{d}_{\mathrm{E-HH,s}} \\ \mathbf{d}_{\mathrm{E-LH,s}} \end{pmatrix}^{\dagger} \begin{pmatrix} \varsigma_n^{\mathrm{HH}} & 0 \\ 0 & \varsigma_n^{\mathrm{LH}} \end{pmatrix} \begin{pmatrix} \mathbf{d}_{\mathrm{E-HH,s}} \\ \mathbf{d}_{\mathrm{E-LH,s}} \end{pmatrix} \cdot \mathbf{E}_{\mathrm{NIR}}, \tag{3}$$

where s labels the twofold degeneracy in the electron-hole states, $\mathbf{d}_{\mathrm{E-HH,s}}$ ($\mathbf{d}_{\mathrm{E-LH,s}}$) is the dipole vector associated with the E-HH (E-LH) states labeled by s, and $\varsigma_n^{\mathrm{HH}}$ ($\varsigma_n^{\mathrm{LH}}$) is a propagator describing the acceleration of the E-HH (E-LH) pairs. The elements i–v of the Michelson interferometer for Bloch waves shown in Fig. 1(c) can be directly identified with the five terms of Eq. (3), reading from right to left.

IV. SEMICLASSICAL THEORY OF BLOCH-WAVE PROPAGATION

In order to better understand the sideband polarizations, and inspired by a semiclassical description of the quasiparticle trajectories [34], we model the propagators ς_n^{ν} ($\nu = \mathrm{HH}, \mathrm{LH}$) with the expression

$$\varsigma_n^{\nu} = \exp\left[i\left(n\omega t_{f,n,\nu} + A_{n,\nu} + (i\Gamma_d + \Delta_{\mathrm{NIR}})\frac{\tau_{n,\nu}}{\hbar}\right)\right], \tag{4}$$

where $\hbar$ is the reduced Planck constant, $\tau_{n,\nu} \equiv t_{f,n,\nu} - t_{o,n,\nu}$ is the time required for an E-H pair to be accelerated by the THz field to gain an energy offset $n\hbar\omega$, with $t_{o,n,\nu}$ and $t_{f,n,\nu}$ being the creation and recombination times associated with a shortest recollision pathway, ω is the angular frequency of the THz field, Γ_d is the dephasing constant of the E-H pairs, $\Delta_{\mathrm{NIR}} \equiv \hbar\Omega - E_g$ is the NIR detuning from the bandgap energy E_g, and $A_{n,\nu}$ is the dynamic phase of the E-H pair accumulated during the acceleration time $\tau_{n,\nu}$. Equation (4) has an oscillating term $e^{i\Theta_\nu(n)}$, where $\Theta_\nu(n) = A_{n,\nu} + n\omega t_{f,n,\nu} + \Delta_{\mathrm{NIR}}\tau_{n,\nu}\hbar^{-1}$, so these propagators oscillate as a function of sideband order with a phase that depends on $A_{n,\nu}$. The presence of $\exp(-\Gamma_d\tau_{n,\nu}\hbar^{-1})$ in Eq. (4) damps the oscillations of the propagators.

Even with this expression for ς_n^{ν}, for a sinusoidal THz field, $\mathbf{E}_{\mathrm{THz}}(t) = F_{\mathrm{THz}}\sin(\omega t)$, there is no analytic solution for $t_{o,n,\nu}$ and $t_{f,n,\nu}$. For experiments reported here, it is reasonable to approximate the THz field as linear in time (LIT) [33],

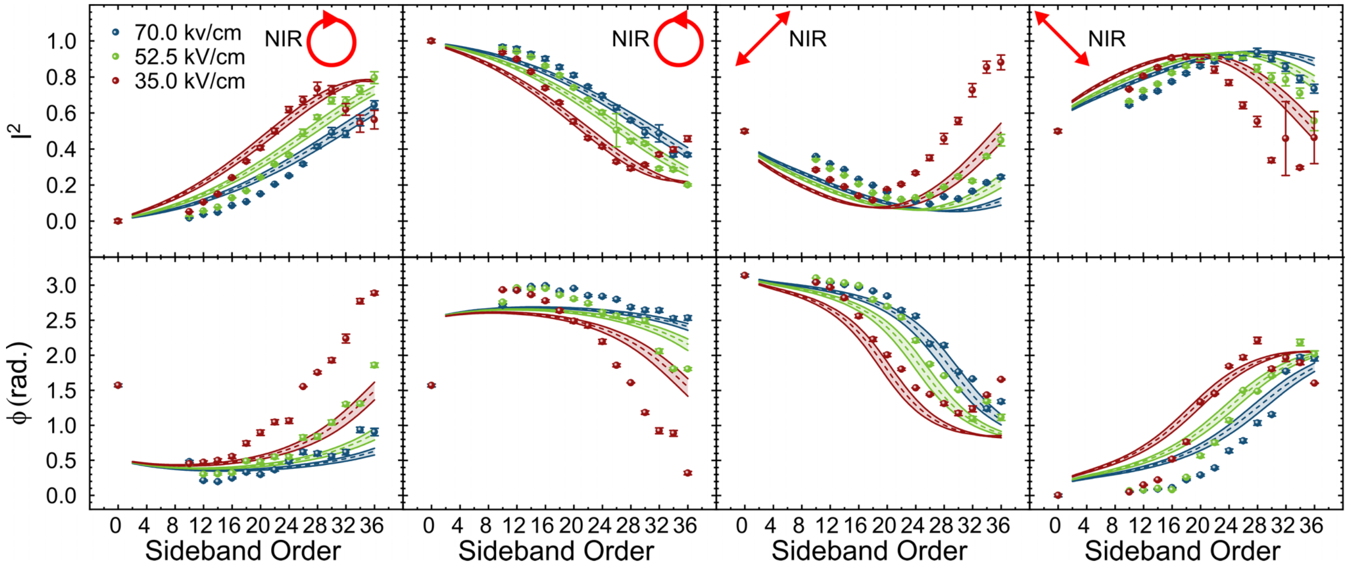

FIG. 2. Bloch-wave interferograms for different NIR polarizations and THz field strengths. (Top row) The left-handed circularly polarized component [$l^2(n)$] [see Eq. (2)]. (Bottom row) The relative phase $\phi(n)$ between the left-handed and right-handed circularly polarized components of the sideband photons. Columns from left to right: four different polarization states of the NIR laser (cartoons in upper corners of top row), right-handed circularly polarized (first), left-handed circularly polarized (second), diagonal (third), and antidiagonal (fourth). The data were taken with three THz field strengths, 70.0 kV/cm (blue symbols), 52.5 kV/cm (green symbols), and 35.0 kV/cm (red symbols). The dashed lines represent the results calculated under the linear-in-time (LIT) approximation, with the bands representing a ±7% experimental error in THz field strength.

because all sidebands arise from E-H pairs accelerated within less than 300 fs of a zero crossing of the THz field, which has a period of 2.2 ps. We may also approximate the electron and hole bands as parabolic because, even for our highest THz fields of 70 kV/cm, the electron-hole pairs explore only about 5% of the Brillouin zone. With the bands approximated as parabolic and the THz field approximated as LIT, $E_{\rm THz} = F_{\rm THz}\omega t$, the following analytic expression for $t_{o,n,\nu}$ and $t_{f,n,\nu}$ can be derived from simple kinematics,

$$-2\omega t_{o,n,\nu} = \omega t_{f,n,\nu} = \frac{2}{\sqrt{3}}\left(\frac{8n\hbar\mu_\nu\omega^3}{e^2F_{\rm THz}^2}\right)^{1/4}. \tag{5}$$

Here, n is the sideband order, μ_ν is the reduced mass of the E-H pair in bulk GaAs, e is the elementary charge, and $F_{\rm THz}$ is the peak THz field strength (see Appendix D for the details). The inverse dependence on field strength means for lower $F_{\rm THz}$, the quasiparticles need to be accelerated for longer times, and thus the E-H pair creation and annihilation times will be farther away from the nodes of the THz field. Because of this, we expect the LIT approximation to be more accurate for higher $F_{\rm THz}$ [33].

In the LIT approximation, we can calculate values for the position, energy, and dynamic phase of a quasiparticle during its acceleration by the THz field (see Appendix D for mathematical details). In this limit, the expression for $A_{n,\nu}$ becomes

$$A_{n,\nu} = -\frac{2\sqrt{3}}{15}\left(\frac{8n^5\hbar\omega^3\mu_\nu}{e^2F_{\rm THz}^2}\right)^{1/4}, \tag{6}$$

which illustrates the dynamic phase's explicit dependence on different experimental variables, and allows us to calculate the dynamics of the Bloch waves in our system. Using Eqs. (3)–(6), we can predict the outgoing sideband polarization from an arbitrary NIR electric field.

V. MEASURED AND CALCULATED BLOCH-WAVE INTERFEROGRAMS

In Fig. 2, we display polarization data, or Bloch-wave interferograms, taken with different THz field strengths and NIR polarization conditions. The top [bottom] row is the measured $l^2(n)$ [$\phi(n)$] recorded at each sideband order. A different NIR polarization is used in each column, depicted with a cartoon in the upper corner. Data were taken at $F_{\rm THz}$ = 70.0, 52.5, and 35.0 kV/cm. Qualitatively, the data demonstrate the behavior predicted by Eq. (3), with $l^2(n)$ and $\phi(n)$ changing with sideband order like a damped sine wave. We define one oscillation of $l^2(n)$ as a fringe in the interferogram, and the amplitude of the first fringe as the fringe contrast. The lower-field-strength data curves oscillate more rapidly with sideband order, following the $F_{\rm THz}^{-1/2}$ dependence of $\tau_{n,\nu}$ and $A_{n,\nu}$ of Eqs. (5) and (6). For the 35-kV/cm data, we observe about half a fringe, and the fringe contrast is about 0.8. The dashed lines in each of the plots are the sideband polarizations predicted from Eq. (3), which can be written as Jones vectors connected by a dynamical Jones matrix [39] T_n in the form,

$$\begin{pmatrix} r(n) \\ l(n)e^{i\phi(n)} \end{pmatrix} \propto \begin{pmatrix} T_{++,n} & T_{+-,n} \\ T_{-+,n} & T_{--,n} \end{pmatrix} \begin{pmatrix} r_{\rm NIR} \\ l_{\rm NIR}e^{i\phi_{\rm NIR}} \end{pmatrix}, \tag{7}$$

where $(r(n), l(n)e^{i\phi(n)})^T$ and $(r_{\rm NIR}, l_{\rm NIR}e^{i\phi_{\rm NIR}})^T$ are the Jones vectors for the nth order sideband and the NIR laser, respectively (see Appendix C 2 for how the electric fields are represented as Jones vectors). The dynamical Jones matrix

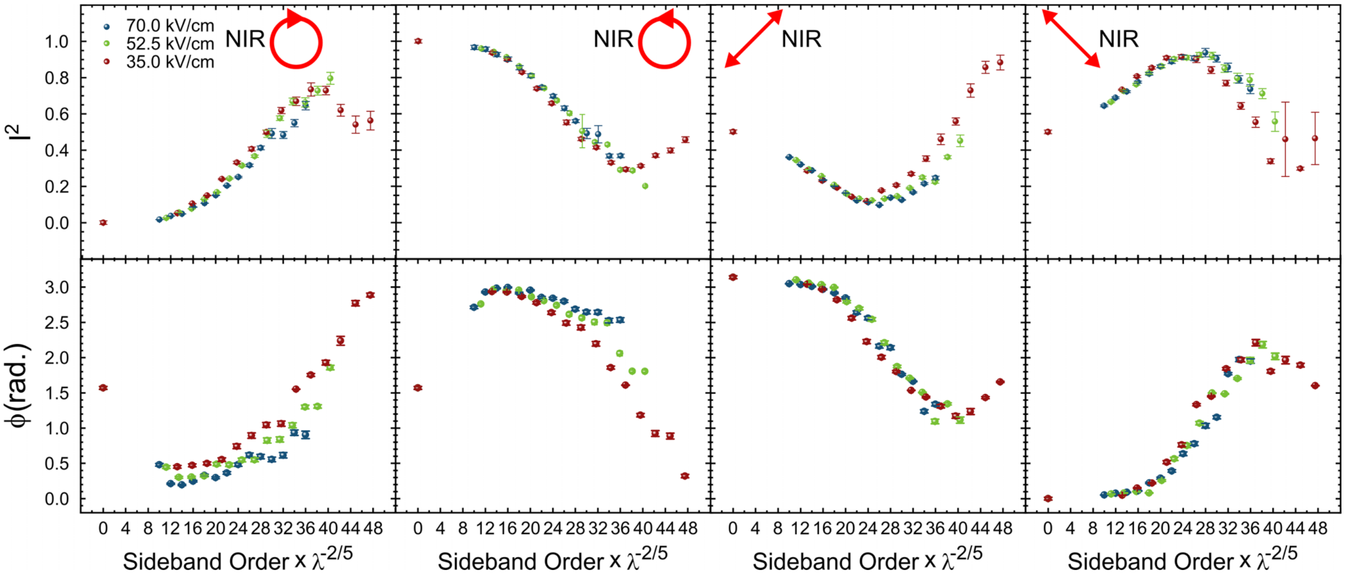

FIG. 3. Scaled Bloch-wave interferograms. The experimental data for $l^2(n)$ and $\phi(n)$ shown in Fig. 2 are plotted as functions of a rescaled sideband order, $n \times \lambda^{-2/5}$ [$\lambda = F_{\mathrm{THz}}/(70\ \mathrm{kV/cm})$], with the scaling factor predicted from Eq. (6).

elements $T_{\pm\pm,n}$ are related to the propagator ς_n^ν ($\nu =$ HH, LH) through the following equations [34]:

$$T_{++,n} = T_{--,n} = \frac{2+n_z}{3}\varsigma_n^{\mathrm{HH}} + \frac{2-n_z}{3}\varsigma_n^{\mathrm{LH}}, \tag{8}$$

$$T_{+-,n} = \frac{n_x + i n_y}{\sqrt{3}}\left(\varsigma_n^{\mathrm{HH}} - \varsigma_n^{\mathrm{LH}}\right), \tag{9}$$

$$T_{-+,n} = \frac{n_x - i n_y}{\sqrt{3}}\left(\varsigma_n^{\mathrm{HH}} - \varsigma_n^{\mathrm{LH}}\right), \tag{10}$$

where $\hat{n} = (n_x, n_y, n_z)$ is a unit vector along the vector $((\sqrt{3}/2)\sin 2\theta, -(\sqrt{3}\gamma_3/2\gamma_2)\cos 2\theta, -1/2)$ that is defined by the angle θ and the two Luttinger parameters, γ_2 and γ_3. Since we can have an analytical form of the propagator ς_n^ν from Eqs. (5) and (6) (see Appendix D for an explicit expression), the dynamical Jones matrix elements can also be calculated analytically. In the calculation, the unit vector $\hat{n}$ and the reduced mass μ_ν were determined by the Luttinger parameters [40], $\gamma_1 = 6.85$, $\gamma_2 = 2.10$, and $\gamma_3 = 2.90$, and the effective mass for the electron band, $m_e = 0.067m_0$, where m_0 is the electron rest mass [41]. The NIR detuning Δ_{NIR} was set to 0 (see Appendix A for a discussion). Only the parameter Γ_d was adjusted to calculate the dashed lines. In principle, the dephasing constants for the E-HH and E-LH pairs could be different and depend on the sideband order. Surprisingly, quantitative agreement between the calculated and measured sideband polarizations can already be achieved by assuming a single dephasing constant with an optimal value of $\Gamma_d = 4.8\hbar\omega$, which was used to calculate all 24 dashed lines in Fig. 2. The positive and negative bands of error represent the $\pm 7\%$ error in THz field strength present in experiment.

VI. A SCALING LAW FOR BLOCH-WAVE INTERFEROGRAMS

In the Michelson interferometer for Bloch waves, both the species-dependent recollision times $t_{f,n,\nu}$ and dynamic phases $A_{n,\nu}$ contribute to the phase difference acquired between Bloch-waves associated with E-LH and E-HH pairs during the acceleration process. The E-LH pairs, because of their smaller reduced mass, take less time to reach the same kinetic energy as the heavier E-HH pairs [see Eq. (5)], and also acquire a smaller dynamic phase [see Eq. (6)].

To illustrate the roles of dynamic phase and recollision time in the Bloch-wave interferograms, we rescale the data in Fig. 3 so that each point on the x-axis is proportional to $\Theta_\nu(n)$, independent of THz field strength. For $\Delta_{\mathrm{NIR}} = 0$, $\Theta_\nu(n) = A_{n,\nu} + n\omega t_{f,n,\nu}$. Examination of Eqs. (5) and (6) shows that both $A_{n,\nu}$ and $n\omega t_{f,n,\nu}$ scale as $(n^5/F_{\mathrm{THz}}{}^2)^{1/4}$. Thus, if the LIT approximation holds, and the NIR laser is tuned sufficiently close to the bandgap such that $\Delta_{\mathrm{NIR}} \approx 0$, we expect that $\Theta_\nu(n)$ should also scale as $(n^5/F_{\mathrm{THz}}{}^2)^{1/4}$. To check this on data sets taken with different THz field strengths, we multiply the sideband order n for each sideband by $\lambda^{-2/5}$, where $\lambda \equiv F_{\mathrm{THz}}/(70\,\mathrm{kV}\cdot\mathrm{cm}^{-1})$. Figure 2 shows that the Bloch-wave interferograms measured with different F_{THz} collapse onto a single curve, in agreement with the predicted LIT scaling law.

VII. DISCUSSION

For the circularly polarized NIR excitations, the calculated value of $l^2(n)$ agrees better with the experimental data than $\phi(n)$, and the $l^2(n)$ curves collapse more completely upon scaling than the $\phi(n)$ curves (see Fig. 3). The opposite is true for the calculated and scaled $l^2(n)$ and $\phi(n)$ for the diagonal and antidiagonal excitation. In fact, the sideband polarizations for different NIR laser polarizations are closely related through Eq. (7). From Eq. (7), we can explicitly calculate $l(n)$ and $\phi(n)$, which define the sideband polarization state, as

$$l^2(n) = \left(1 + \left|\frac{T_{++,n}r_{\mathrm{NIR}} + T_{+-,n}l_{\mathrm{NIR}}e^{i\phi_{\mathrm{NIR}}}}{T_{-+,n}r_{\mathrm{NIR}} + T_{--,n}l_{\mathrm{NIR}}e^{i\phi_{\mathrm{NIR}}}}\right|^2\right)^{-1}, \tag{11}$$

$$\phi(n) = \arg\left[\frac{T_{-+,n}r_{\mathrm{NIR}} + T_{--,n}l_{\mathrm{NIR}}e^{i\phi_{\mathrm{NIR}}}}{T_{++,n}r_{\mathrm{NIR}} + T_{+-,n}l_{\mathrm{NIR}}e^{i\phi_{\mathrm{NIR}}}}\right] (\mathrm{mod}\ 2\pi). \tag{12}$$

As shown by these expressions, for a fixed polarization state of the NIR laser, the polarization state of the nth-order sideband is fully determined by the three ratios of the dynamical Jones matrix elements, $T_{++,n}/T_{--,n}$, $T_{+-,n}/T_{--,n}$, and $T_{-+,n}/T_{--,n}$. For unstrained or weakly strained bulk GaAs sample, with the relations discovered in Ref. [34],

$$T_{++,n} = T_{--,n}, \tag{13}$$

$$\frac{T_{+-,n}}{T_{-+,n}} \equiv \chi_n(\theta) = \frac{\gamma_2 \sin(2\theta) - i\gamma_3 \cos(2\theta)}{\gamma_2 \sin(2\theta) + i\gamma_3 \cos(2\theta)}, \tag{14}$$

we can further simply Eqs. (11) and (12) as

$$l^2(n) = \left(1 + \left|\frac{\rho_n r_{\rm NIR} + \chi_n(\theta) l_{\rm NIR} e^{i\phi_{\rm NIR}}}{r_{\rm NIR} + \rho_n l_{\rm NIR} e^{i\phi_{\rm NIR}}}\right|^2\right)^{-1}, \tag{15}$$

$$\phi(n) = \arg\left[\frac{r_{\rm NIR} + \rho_n l_{\rm NIR} e^{i\phi_{\rm NIR}}}{\rho_n r_{\rm NIR} + \chi_n(\theta) l_{\rm NIR} e^{i\phi_{\rm NIR}}}\right] (\bmod 2\pi). \tag{16}$$

Here, we have defined $\rho_n \equiv T_{++,n}/T_{-+,n}$, which is now the only complex parameter that fully determine the polarization state of the nth-order sideband. From Eqs. (15) and (16), one can easily see that, by measuring $l^2(n)$ and $\phi(n)$ for a certain polarization state of the NIR laser, the ratio ρ_n can be determined and used to predict the polarization states of sidebands for any other NIR laser polarizations.

To be specific, using a right-handed circularly polarized (RHCP) NIR laser, we have $r_{\rm NIR} = 1$ and $l_{\rm NIR} = 0$ so that

$$l^2_{\rm RHCP}(n) = \frac{1}{1 + |\rho_n|^2}, \tag{17}$$

$$\phi_{\rm RHCP}(n) = -\arg[\rho_n] (\bmod 2\pi), \tag{18}$$

which give

$$\rho_n = \sqrt{\frac{1 - l^2_{\rm RHCP}(n)}{l^2_{\rm RHCP}(n)}} \exp[-i\phi_{\rm RHCP}(n)]. \tag{19}$$

Therefore, the results presented in the first column of Fig. 2 can be used to predict the data in the rest of the figure. In particular, the discrepancies between theory and experiment in the first column of Fig. 2 can be used to predict the discrepancies in other columns.

For simplicity, we now approximate the angle θ to be 90 degrees such that $\chi_n(\theta) = -1$. For a left-handed circularly polarized (LHCP) NIR laser, we have $r_{\rm NIR} = 0$ and $l_{\rm NIR} = 1$ so that

$$l^2_{\rm LHCP}(n) = \frac{|\rho_n|^2}{1 + |\rho_n|^2}, \tag{20}$$

$$\phi_{\rm LHCP}(n) = \arg[\rho_n] + \pi (\bmod 2\pi), \tag{21}$$

which are consistent with the observation from the first two columns of Fig. 2 that

$$l^2_{\rm RHCP}(n) + l^2_{\rm LHCP}(n) \approx 1, \tag{22}$$

$$\phi_{\rm RHCP}(n) + \phi_{\rm LHCP}(n) \approx \pi (\bmod 2\pi). \tag{23}$$

For the diagonal (D_+) and antidiagonal (D_-) NIR excitations (last two columns of Fig. 2), we have $r_{\rm NIR} = 1/\sqrt{2}$ and $l_{\rm NIR} = \mp 1/\sqrt{2}$ so that

$$l^2_{D_\pm}(n) = \frac{|1 \mp \rho_n|^2}{|1 \mp \rho_n|^2 + |1 \pm \rho_n|^2}, \tag{24}$$

$$\phi_{D_\pm}(n) = \arg\left[\frac{1 \mp \rho_n}{\rho_n \pm 1}\right] (\bmod 2\pi), \tag{25}$$

which are consistent with the results shown in the last two columns of Fig. 2. For example, we observe the relations

$$l^2_{D_+}(n) + l^2_{D_-}(n) \approx 1, \tag{26}$$

$$\phi_{D_+}(n) + \phi_{D_-}(n) \approx \pi (\bmod 2\pi). \tag{27}$$

The deviation between theory and experiment for the RHCP NIR excitation can also be used to infer those deviations for other NIR excitations. For example, consider why theory and experiment agree better in $\phi_{D_+}(n)$ than $l^2_{D_+}(n)$ for a sideband, say 22th order sideband produced by a 35.0 kV/cm THz field (the third column of Fig. 2). Using the fact that the value of $l^2_{\rm RHCP}(22)$ is about 0.5 for both theory and experiment (the first column of Fig. 2), we can predict that $\phi_{D_+}(22)$ should be about $\pi/2$, insensitive to the value of $\phi_{\rm RHCP}(22)$, since $(1 - \rho_{22})/(\rho_{22} + 1)$ is close to a pure imaginary number with $|\rho_{22}| \approx 1$ [see Eq. (25)]. In contrast, as can be seen from Eqs. (24) and (19), $l^2_{D_+}(n)$ is sensitive to the deviation in $\phi_{\rm RHCP}(n)$, which is a finite value of about 0.5 rad at $n = 22$ (the first column of Fig. 2). For all sidebands of orders $n > 20$ for the RHCP NIR excitation, $l^2_{\rm RHCP}(n)$ ranges from about 0.2 to 0.8 for both theory and experiment (the first column of Fig. 2), corresponding to the value of ρ_n going from about 2 to 0.5, which implies that the $\phi_{D_+}(n)$ curves for $n > 20$ should lie around $\pi/2$ for both theory and experiment as shown in the third column of Fig. 2. The analysis for the anti-diagonal NIR excitation is similar.

VIII. CONCLUSIONS

The success of the scaling demonstrated in Fig. 3, together with the agreement between calculated and measured Bloch-wave interferograms shown in Fig. 2, strongly support our assertion that the HSG process in bulk GaAs can be viewed as a Michelson interferometer for Bloch waves.

By taking into account the effects of quantum fluctuations and going beyond the LIT approximation as in Ref. [33], and by allowing additional free parameters—for example, detuning $\Delta_{\rm NIR}$, μ_ν different from those predicted by literature values of the Luttinger parameters, dephasing varying with sideband order, and the influence of unavoidable small strain lifting the degeneracy between HH and LH at the center of the Brillouin zone (see Appendix A for a discussion)—future analysis will increase the agreement of the other variables measured in experiment, and reveal some physics left out in the simplest nontrivial approximations made in this paper.

By leveraging the flexibility of HSG to create carefully selected superpositions of charged quasiparticles by controlling the polarization and frequency of the NIR laser while independently choosing the field strength and frequency of the THz laser, we have been able to create a Michelson interferometer for Bloch waves. Given the frequency and field strength of the THz laser, the analytic model we presented directly connects the experimentally observed sideband polarizations with the inertial properties of charged quasiparticles. We note that the values of effective masses extracted via Bloch wave interferometry are those associated with the direction of electron and hole motion—they are not averaged over all directions, as are those extracted from cyclotron resonance [42]. Nonequilibrium dephasing of electron-hole pairs can be used to probe their interactions with phonons [43], disorder and, if sufficiently high NIR powers are used, correlations with other electron-hole pairs. Finally, future experiments could be used to measure other important materials parameters with increased precision and specificity. For example, the bandgap of a direct-gap semiconductor is difficult to extract directly from an absorption measurement because of excitonic features. Equation (4) includes the detuning Δ_{NIR} as a parameter, which we have set to zero in this paper. By allowing this parameter to vary in a systematic study, a more precise value of the semiconducting bandgap could be determined. Bloch-wave interferometry thus has the potential to become an important new tool for determining the electronic structure of strongly driven quantum condensed matter.

ACKNOWLEDGMENTS

The work reported here was funded by NSF DMR 2004995 and NSF DMR 2333941. We thank David Weld for helpful discussions, and Audrina Sewal for participation in experiments.

APPENDIX A: STRAINS IN THE SAMPLE

Strain can distort the band structure of GaAs and introduce non-Abelian Berry curvatures into the dynamics of electron-hole pairs in the HSG experiment [34]. Minimizing the strain in the sample is important to minimize Berry curvatures, which are not included in the Bloch-wave interferometry picture presented here. Making the strain uniform over the size of the NIR beam spot is important to ensure that sideband polarization does not vary across the beam spot.

To ensure that the NIR beam spot covers an area with a sufficiently uniform and minimal strain, absorbance measurements were performed with a white light source to examine the local strain environment of the GaAs epilayer under the conditions for the HSG experiment. Figure 4 shows an example of an absorbance spectrum, where there are two absorbance peaks associated with different hole spins. The peak splitting arises from the lifting of degeneracy between the heavy-hole (HH) and light-hole (LH) bands due to strain. Such strain-induced exciton splittings were observed in all low-temperature measurements of the absorbance of bulk GaAs films glued or bonded to substrates as far as we know from the literature—see, for example, Ref. [44]. After one absorbance spectrum was recorded, the sample was translated by a fraction of the size of the white light beam spot and the absorbance was measured again. This process was repeated over a 7 mm×3 mm section of the sample to find a region with the highest absorbance peak and the most uniform absorbance peak splitting compared to its nearby regions. The region chosen for the HSG experiment is displayed in the inset of Fig. 4, along with the absorbance spectrum.

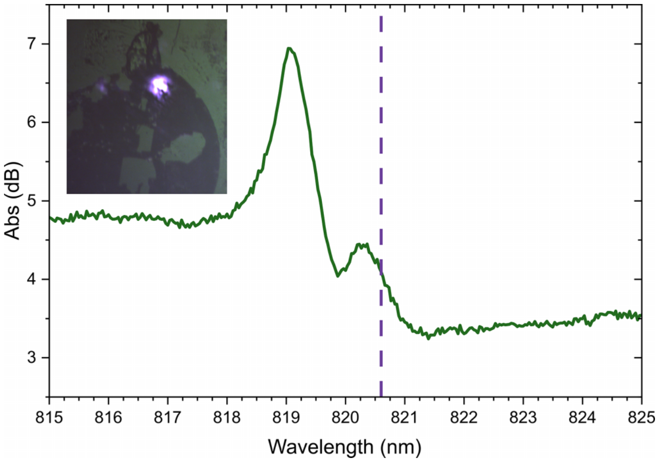

FIG. 4. An absorbance spectrum of the GaAs epilayer. The purple dashed line indicates the NIR wavelength used in experiments reported in this paper. The measurement was taken at the spot illuminated by a white light source (inset).

As a result of the small strain-induced splitting between LH and HH bands ($\delta_{\mathrm{HH-LH}} < 3$ meV) shown in Fig. 4, the detunings Δ_{NIR} are different for electron-hole (E-H) pair excitations associated with different hole spins. The magnitude of such differences are on the same scale as $\delta_{\mathrm{HH-LH}}$, much less than typical sideband offset energies. For this reason, in this paper, we simply set $\Delta_{\mathrm{NIR}} = 0$. In a future paper, we will attempt to separately extract the gaps for the E-HH and E-LH pairs.

APPENDIX B: THZ FIELD STRENGTH AT GaAs EPILAYER

Because of the importance of the THz field strengths to our results, care was taken to track the THz field strength during the HSG experiment. The THz field strength was constantly monitored by a pyroelectric detector, whose response was calibrated by a Thomas-Keating (TK) absolute power/energy meter before HSG experiment each day. A beam splitter directed 10% of the THz power into the pyroelectric detector, allowing for pulse-by-pulse monitoring while HSG experiments were performed. After the THz beam passed the position at which the TK meter was placed, the THz field was reflected by a flat mirror, a gold-coated off-axis parabolic mirror, and an ITO slide, then transmitted though the cryostat window, and reflected by the ITO coating on the sapphire substrate to build up field enhancement at the GaAs epilayer. In the calculation of the THz field strength, we assume the gold-coated off-axis parabolic mirror and flat mirror are 100% reflective, the ITO slide 70% reflective, the cryostat window 95% transmissive, and the ITO coating on the sapphire provides a 150% field enhancement at the GaAs epilayer. This gives a relative field strength of 99.75% at the GaAs epilayer with respect to that deduced from the pyroelectric detector signal (see Ref. [34] for details).

Two wire grid polarizers were used to attenuate the THz field at the GaAs epilayer to 75% and 50% of the peak field strength $F_{\mathrm{THz},0} = 70$ kV/cm by adjusting the relative angle, Φ, between the two wire grids, while maintaining the horizontal polarization of the THz field. The equation $F_{\mathrm{THz}}(\Phi) = F_{\mathrm{THz},0}\cos^2(\Phi)$ was used to calculate the THz field strength at the GaAs epilayer for an angle Φ set by a motorized rotation mount. Prior to the HSG experiment, the TK power detector, placed downstream of the wire grid polarizers, was used to calibrate the motor settings and determine the configuration for $\Phi = 0$.

APPENDIX C: STOKES POLARIMETRY

The polarization of the sideband electric fields were measured by using Stokes polarimetry. We obtained, for each sideband, four Stokes parameters, from which the sideband electric field was represented in a basis of circularly polarized fields, as shown in Fig. 1(d).

1. Stokes parameters

The optical setup is detailed in Refs. [34,39]. The NIR and THz lasers were simultaneously and collinearly focused onto the GaAs sample, leading to generation of high-order sidebands. The sidebands were transmitted out of the cryostat and propagated through the Stokes polarimeter, which consists of a quarter-wave plate (QWP) mounted on a rotation stage and a horizontal linear polarizer.

The sidebands were then coupled into a grating spectrometer and detected with an electron-multiplied CCD (charge-coupled device) camera. The lowest orders of sidebands were cut off by a short-pass optical filter to filter out the NIR laser, which was about 10^5 more intense than the strongest sideband fields. For the experiments reported in this paper, the 10th-order sideband is the lowest-order sideband to be resolved, and the 36th-order is the highest.

The relative intensities of the sidebands measured through the CCD camera $S_{0,\mathrm{out}}$ are dependent on the Stokes parameters S_i ($i = 0, 1, 2, 3$), and the orientation angle of the QWP fast axis with respect to the horizontal θ_{QWP} following the expression

$$S_{0,\mathrm{out}}(\theta_{\mathrm{QWP}}) = \frac{S_0}{2} + \frac{S_1}{4} - \frac{S_3}{2}\sin 2\theta_{\mathrm{QWP}} + \frac{S_1}{4}\cos 4\theta_{\mathrm{QWP}} + \frac{S_2}{4}\sin 4\theta_{\mathrm{QWP}}. \tag{C1}$$

In the Stokes polarimetry experiment, $S_{0,\mathrm{out}}$ of each sideband was measured with the angle θ_{QWP} sweeping from 0 to 360 degrees in 22.5-degree steps. The four Stokes parameters were then calculated from Fourier transforms of $S_{0,\mathrm{out}}$ with respect to the angle θ_{QWP}, as detailed in Ref. [34].

2. Representation of the sideband electric field

To conveniently make a comparison between theory and experiment, we choose the basis of circular polarization fields as

$$|R\rangle = \frac{\hat{X} + i\hat{Y}}{\sqrt{2}}, \tag{C2}$$

$$|L\rangle = -\frac{\hat{X} - i\hat{Y}}{\sqrt{2}}, \tag{C3}$$

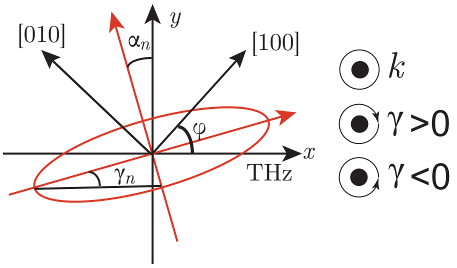

FIG. 5. Definition of the orientation angle α_n and ellipticity angle γ_n. The sign of the ellipticity angle γ_n is defined with respect to the wave vector k.

with $\hat{X}$ ($\hat{Y}$) being a unit vector along [001] ([010]) crystal axis of bulk GaAs, and write the polarization state of the nth-order sideband as

$$|E_{\mathrm{SB},n}\rangle = l(n)e^{i\phi(n)}|L\rangle + r(n)|R\rangle, \tag{C4}$$

where the functions $l(n)$, $r(n)$, and $\phi(n)$ are all real, and satisfy $l^2(n) + r^2(n) = 1$.

The polarization state $|E_{\mathrm{SB},n}\rangle$ can be determined by the Stokes parameters through the orientation angle α_n and ellipticity angle γ_n defined with respect to the horizontal polarization of the THz field (see Fig. 5 for the definition). The Jones vector associated with the polarization state $|E_{\mathrm{SB},n}\rangle$ can be written as

$$\begin{pmatrix} E_{x,n} \\ E_{y,n} \end{pmatrix} \propto \begin{pmatrix} \cos\alpha_n\cos\gamma_n - i\sin\alpha_n\sin\gamma_n \\ \sin\alpha_n\cos\gamma_n + i\cos\alpha_n\sin\gamma_n \end{pmatrix}, \tag{C5}$$

with the x axis defined by the horizontal polarization of the THz field. The Jones vector in the basis $\{|R\rangle, |L\rangle\}$ can be related to the Jones vector $(E_{x,n}, E_{y,n})^T$ through a unitary transformation,

$$\begin{pmatrix} r(n) \\ l(n)e^{i\phi(n)} \end{pmatrix} \propto \frac{1}{\sqrt{2}} \begin{pmatrix} e^{i\varphi} & -ie^{i\varphi} \\ -e^{-i\varphi} & -ie^{-i\varphi} \end{pmatrix} \begin{pmatrix} E_{x,n} \\ E_{y,n} \end{pmatrix}, \tag{C6}$$

where φ is the angle between the [100] crystal axis and the linear polarization of the THz field. After some algebra, we obtain

$$r^2(n) = \frac{1 + \sin 2\gamma_n}{2}, \tag{C7}$$

$$l^2(n) = \frac{1 - \sin 2\gamma_n}{2}, \tag{C8}$$

$$\phi(n) = 2(\alpha_n - \varphi) + \pi \ (\mathrm{mod}\, 2\pi). \tag{C9}$$

Using the relations connecting the Stokes parameters with the angles α_n and γ_n [34],

$$\sin 2\gamma_n = \frac{S_3}{S_1^2 + S_2^2 + S_3^2}, \tag{C10}$$

$$\tan 2\alpha_n = \frac{S_2}{S_1}, \tag{C11}$$

we arrive at the equations

$$r^2(n) = \frac{1+\tilde{S}_3}{2}, \tag{C12}$$

$$l^2(n) = \frac{1-\tilde{S}_3}{2}, \tag{C13}$$

$$\phi(n) = \arctan\frac{\tilde{S}_2}{\tilde{S}_1} - 2\theta - \pi/2\,(\mathrm{mod}\,2\pi), \tag{C14}$$

where θ is the angle between the [110] crystal axis and the linear polarization of the THz field, and the Stokes parameters, S_1, S_2, and S_3, are normalized as $\tilde{S}_j = S_j/\sqrt{S_1^2+S_2^2+S_3^2}$ ($j = 1, 2, 3$).

APPENDIX D: THEORY OF SIDEBAND POLARIZATION

To calculate the sideband polarization, we need a model for the propagators describing recollisions of the E-HH and E-LH pairs. Following Ref. [34], we start with the expression for the propagators,

$$\varsigma_n^{\mathrm{HH(LH)}} = \int_0^{\frac{2\pi}{\omega}} dt\, e^{i(\Omega+n\omega)t} \cdot \times \int_{-\infty}^{t} dt' e^{i[-E_g(t-t')/\hbar + A_{\mathrm{HH(LH)}}(t,t')]-(\Gamma_d/\hbar)(t-t')} \times e^{-i\Omega t'}, \tag{D1}$$

where Ω and ω are the angular frequencies of the NIR laser and THz field, respectively, Γ_d is the dephasing constant, $\hbar$ is the reduced Planck constant, and

$$A_{\mathrm{HH(LH)}}(t,t') = -\int_t^{t'} dt'' \frac{\hbar \mathbf{k}^2(t'')}{2\mu_{\mathrm{HH(LH)}}} \tag{D2}$$

is the dynamic phase acquired by the E-HH (E-LH) pairs from the time t to t' with the contribution from the bandgap E_g subtracted, and μ_{HH} (μ_{LH}) is the reduced mass of the E-HH (E-LH) pairs. The integral includes all recollision pathways starting from $\mathbf{k} = 0$.

1. Semiclassical Theory of SB Polarization

Inspired by the semiclassical description given in Ref. [34] and Ref. [33], we assume that, for each species of E-H pair, there is one shortest recollision pathway that dominantly determines the polarization of a sideband. Taking the integration variables t' and t as the creation and recombination times associated with a shortest recollision pathway, $t_{o,n,\nu}$ and $t_{f,n,\nu}$ (ν = HH, LH), and neglecting all quantum fluctuations, we model the propagators as

$$\varsigma_n^{\nu} = e^{i[n\omega t_{f,n,\nu} + A_{n,\nu} + (i\Gamma_d + \Delta_{\mathrm{NIR}})\tau_{n,\nu}/\hbar]}, \tag{D3}$$

where $\tau_{n,\nu} \equiv t_{f,n,\nu} - t_{o,n,\nu}$ is the time duration, $\Delta_{\mathrm{NIR}} = \hbar\Omega - E_g$ is the detuning of the NIR laser, and $A_{n,\nu} = A_\nu(t_{f,n,\nu}, t_{o,n,\nu})$. Here, the recollision processes are considered to be fully classical. We set $\Delta_{\mathrm{NIR}} = 0$ for simplicity as mentioned earlier.

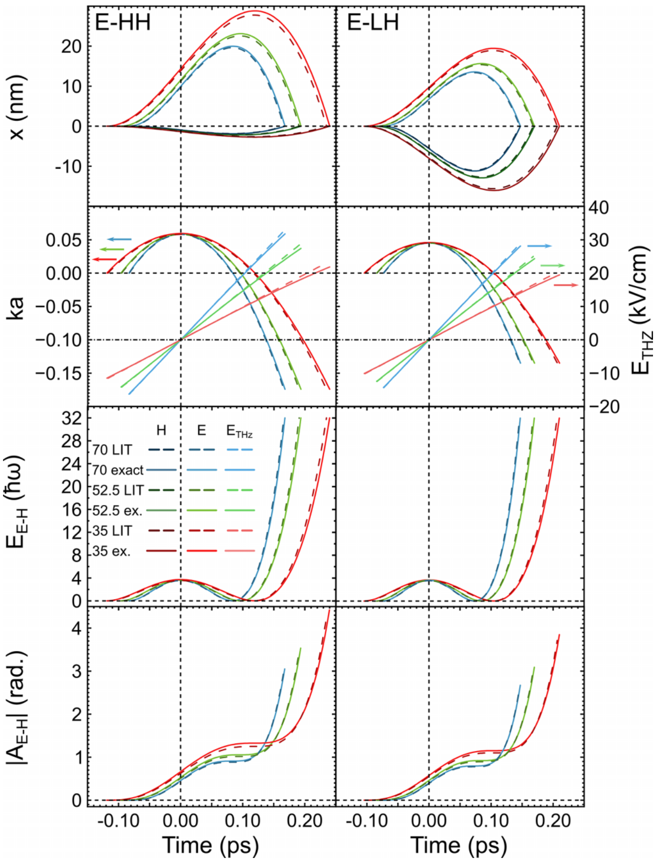

FIG. 6. Dynamical quantities calculated by using the LIT approximation (dashed line) and the numerical solutions with a sinusoidal (solid line) THz field for the E-H pairs, which produce a 32nd-order sideband. The results for different field strengths used in the experiment, 70 kV/cm (blue), 52.5 kV/cm (green), and 35 kV/cm (red), are all displayed. The left and right columns show quantities calculated for the E-HH and E-LH pairs, respectively. The top row shows the calculated x position for the holes (dark colors) and electrons (light colors). The second row shows the calculated wave vectors for the electrons (downward parabolas, associated with the left y axis, a = 5.56 Å) and the THz fields (lines, associated with the right y axis). The third row shows the calculated kinetic energies of the E-H pairs. The bottom row shows the calculated absolute values of the dynamic phases of the E-H pairs.

2. Classical trajectories

To obtain the creation and recombination times, $t_{o,n,\nu}$ and $t_{f,n,\nu}$ (ν = HH, LH), we start with the Newton's equation of motion, $\hbar\dot{k} = -eE_{\mathrm{THz}}(t)$, with e being the elementary charge and a sinusoidal THz field in the form $E_{\mathrm{THz}}(t) = F_{\mathrm{THz}}\sin(\omega t)$. Taking the initial condition $k(t_{o,n,\nu}) = 0$, we obtain the solution for the momentum,

$$\hbar k(t) = \frac{eF_{\mathrm{THz}}}{\omega}[\cos(\omega t) - \cos(\omega t_{o,n,\nu})]. \tag{D4}$$

The positions of the electrons and holes are then given by

$$x(t)=\int_{t_{o,n,\nu}}^{t} dt'' \frac{\hbar k(t'')}{m} = \frac{-eF_{\mathrm{THz}}}{m\omega^2}[\omega(t-t_{o,n,\nu})\cos(\omega t_{o,n,\nu}) + \sin(\omega t_{o,n,\nu}) - \sin(\omega t)], \tag{D5}$$

where m is the effective mass. Using the energy conservation equation, $\hbar^2k^2(t_{f,n,\nu})/(2\mu_\nu)=n\hbar\omega$, and the condition that, at recollision, the electrons and holes return to the origin, $x(t_{f,n,\nu})=0$, one can solve the times $t_{o,n,\nu}$ and $t_{f,n,\nu}$ numerically (see, for example, Ref. [33]).

3. The linear-in-time (LIT) approximation

To further simplify the analysis, we notice, from the classical recollision picture that, all sidebands observed in this paper can be attributed to electron-hole recollisions occurring within less than 250 fs after a zero-crossing of the THz field (see Fig. 6), whereas the THz field used in HSG experiment has a period of 2.22 ps. Thus we make the approximation that the THz field is linear in time (LIT),

$$E_{\mathrm{THz}}(t)\approx F_{\mathrm{THz}}\omega t. \tag{D6}$$

The LIT approximation has been applied to solve the semiclassical trajectories of E-H pairs in HSG [33]. For the special case of classical recollisions, the creation and recombination times, $t_{o,n,\nu}$ and $t_{f,n,\nu}$ ($\nu=\mathrm{HH},\mathrm{LH}$) satisfy [33]

$$-2\omega t_{o,n,\nu}=\omega t_{f,n,\nu}=\frac{2}{\sqrt{3}}\left(\frac{2nE_{\mathrm{ph}}}{U_\nu}\right)^{1/4}, \tag{D7}$$

where E_{ph} is the THz photon energy, and $U_\nu=e^2F_{\mathrm{THz}}^2/(4\mu_\nu\omega^2)$ is the ponderomotive energy. Within the LIT approximation, the momentum $\hbar k(t)$ and the positions of the electron-hole pairs are all polynomials as functions of time,

$$\hbar k(t)=\frac{eF_{\mathrm{THz}}}{2\omega}[(\omega t_{o,n,\nu})^2-(\omega t)^2], \tag{D8}$$

$$x(t)=\frac{-eF_{\mathrm{THz}}}{2m\omega^2}\left[\left(\frac{1}{3}\omega t\right)^3-(\omega t_{o,n,\nu})^2\omega t+\frac{2}{3}(\omega t_{o,n,\nu})^3\right]. \tag{D9}$$

The solution of $t_{o,n,\nu}$ and $t_{f,n,\nu}$ [Eq. (D7)] can be derived from the conditions $x(t_{f,n,\nu})=0$ and $\hbar^2k^2(t_{f,n,\nu})/(2\mu_\nu)=n\hbar\omega$.

4. Calculation of the propagators

With the linear-in-time approximation, using the solutions of the creation and recombination times, $t_{o,n,\nu}$ and $t_{f,n,\nu}$ ($\nu=$ HH, LH), we obtain the dynamic phase using Eq. (D2),

$$A_{n,\nu}=-\frac{2\sqrt{3}}{15}\left(\frac{8n^5\hbar\omega^3\mu_\nu}{e^2F_{\mathrm{THz}}^2}\right)^{1/4}. \tag{D10}$$

The propagators are then calculated by using Eq. (D3) as

$$\varsigma_n^\nu=\exp\left[i\left(\frac{8n}{15}+\left(\frac{i\Gamma_d+\Delta_{\mathrm{NIR}}}{\hbar\omega}\right)\right)\left(\frac{72n\hbar\omega^3\mu_\nu}{e^2F_{\mathrm{THz}}^2}\right)^{1/4}\right]. \tag{D11}$$

5. Accuracy of LIT approximation

We compare the values of position $x(t)$, wave vector $k(t)$, kinetic energy $E_{e-\nu}(t)=\hbar^2k^2(t)/(2\mu_\nu)$, and dynamic phase $A_{n,\nu}$ ($\nu=$ HH, LH), calculated by using the LIT approximation and the numerical solutions by using $E_{\mathrm{THZ}}(t)=F_{\mathrm{THz}}\sin(\omega t)$ (sinusoidal THz field). Figure 6 demonstrates the accuracy of the LIT approximation for time domains relevant to the sideband generation observed in the experiment.

[1] A. A. Michelson and E. W. Morley, Am. J. Sci. **s3-34**, 333 (1887).

[2] G. P. Thomson and A. Reid, Nature (London) **119**, 890 (1927).

[3] C. J. Davisson and L. H. Germer, Proc. Natl. Acad. Sci. USA **14**, 317 (1928).

[4] O. Carnal and J. Mlynek, Phys. Rev. Lett. **66**, 2689 (1991).

[5] M. Kasevich and S. Chu, Appl. Phys. B **54**, 321 (1992).

[6] Y. Hasegawa and P. Avouris, Phys. Rev. Lett. **71**, 1071 (1993).

[7] M. F. Crommie, C. P. Lutz, and D. M. Elgler, Nature (London) **363**, 524 (1993).

[8] E. J. Heller, M. F. Crommie, C. P. Lutz, and D. M. Elgler, Nature (London) **369**, 464 (1994).

[9] A. Yacoby, M. Heiblum, V. Umansky, H. Shtrikman, and D. Mahalu, Phys. Rev. Lett. **73**, 3149 (1994).

[10] Y. Ji, Y. Chung, D. Sprinzak, M. Heiblum, D. Mahalu, and H. Shtrikman, Nature (London) **422**, 415 (2003).

[11] P. M. Paul, E. S. Toma, P. Breger, G. Mullot, F. Augé, P. Balcou, H. G. Muller, and P. Agostini, Science **292**, 1689 (2001).

[12] N. Dudovich, O. Smirnova, J. Levesque, Y. Mairesse, M. Y. Ivanov, D. M. Villeneuve, and P. B. Corkum, Nat. Phys. **2**, 781 (2006).

[13] G. Vampa, T. J. Hammond, N. Thiré, B. E. Schmidt, F. Légaré, C. R. McDonald, T. Brabec, and P. B. Corkum, Nature (London) **522**, 462 (2015).

[14] T. T. Luu, M. Garg, S. Y. Kruchinin, A. Moulet, M. T. Hassan, and E. Goulielmakis, Nature (London) **521**, 498 (2015).

[15] E. Goulielmakis and T. Brabec, Nat. Photon. **16**, 411 (2022).

[16] N. Tancogne-Dejean, M. A. Sentef, and A. Rubio, Phys. Rev. Lett. **121**, 097402 (2018).

[17] L. Yue and M. B. Gaarde, J. Opt. Soc. Am. B **39**, 535 (2022).

[18] M. Hohenleutner, F. Langer, O. Schubert, M. Knorr, U. Huntner, S. W. Koch, M. Kira, and R. Huber, Nature (London) **523**, 572 (2015).

[19] M. Garg, M. Zhan, T. T. Luu, H. Lakhotia, T. Klostermann, A. Guggenmos, and E. Goulielmakis, Nature (London) **538**, 359 (2016).

[20] A. J. Uzan, G. Orenstein, Á. Jiménez-Galán, C. McDonald, R. E. F. Silva, B. D. Bruner, N. D. Klimkin, V. Blanchet, T. Arusi-Parpar, M. Krüger *et al.*, Nat. Photon. **14**, 183 (2020).

[21] Y. S. You, D. A. Reis, and S. Ghimire, Nat. Phys. **13**, 345 (2017).

[22] H. Liu, Y. Li, Y.-S. You, S. Ghimire, T. F. Heinz, and D. A. Reis, Nat. Phys. **13**, 262 (2017).

[23] N. Yoshikawa, T. Tamaya, and K. Tanaka, Science **356**, 736 (2017).

[24] A. J. Uzan-Narovlansky, Á. Jiménex-Galán, G. Orenstein, R. F. Silva, T. Arusi-Parpar, S. Shames, B. D. Bruner, B. Yan, O. Smirnova, M. Ivanov, and N. Dudovich, Nat. Photon. **16**, 428 (2022).

[25] L. Li, P. Lan, X. Zhu, and P. Lu, Phys. Rev. Lett. **127**, 223201 (2021).

[26] B. Zaks, R. B. Liu, and M. S. Sherwin, Nature (London) **483**, 580 (2012).

[27] B. Zaks, H. B. Banks, R. B. Liu, and M. Sherwin, Ap. Phys. Lett. **102**, 012104 (2013).

[28] H. B. Banks, B. Zaks, F. Yang, S. Mack, A. C. Gossard, R. B. Liu, and M. S. Sherwin, Phys. Rev. Lett. **111**, 267402 (2013).

[29] F. Langer, M. Hohenleutner, C. P. Schmid, C. Poellmann, P. Naggler, T. Korn, C. Schüller, M. S. Sherwin, U. Hunter, J. T. Steiner, S. W. Koch, M. Kira, and R. Huber, Nature (London) **533**, 225 (2016).

[30] F. Langer, C. P. Schmid, S. Schlauderer, M. Gmitra, J. Fabian, P. Nagler, C. Schüller, T. Korn, P. G. Hawkins, J. T. Steiner *et al.*, Nature (London) **557**, 76 (2018).

[31] D. Valovcin, H. B. Banks, S. Mack, A. C. Gossard, K. West, L. Pfeiffer, and M. S. Sherwin, Opt. Express **26**, 29807 (2018).

[32] J. Freudenstein, M. Borsch, M. Meierhofer, D. Afanaslev, C. P. Schmid, F. Sandner, M. Liebich, A. Girnghuber, M. Knorr, M. Kira, and R. Huber, Nature (London) **610**, 290 (2022).

[33] Q. Wu and M. S. Sherwin, Phys. Rev. B **107**, 174308 (2023).

[34] J. B. Costello, S. D. O'Hara, Q. Wu, D. Valovcin, K. West, L. Pfeiffer, and M. Sherwin, Nature (London) **599**, 57 (2021).

[35] E. Yablonovitch, T. Gmitter, J. P. Harbison, and R. Bhat, Appl. Phys. Lett. **51**, 2222 (1987).

[36] E. Yablonovitch, D. M. Hwang, T. J. Gmitter, L. T. Florez, and J. P. Harbison, Appl. Phys. Lett. **56**, 2419 (1990).

[37] G. D. Cole, W. Zhang, M. J. Martin, J. Ye, and M. Aspelmeyer, Nat. Photon. **7**, 644 (2013).

[38] G. D. Cole, W. Zhang, B. J. Bjork, D. Follman, P. Heu, C. Deutsch, L. Sonderhouse, J. Robinson, C. Franz, A. Alexandrovski *et al.*, Optica **3**, 647 (2016).

[39] H. B. Banks, Q. Wu, D. C. Valovcin, S. Mack, A. C. Gossard, L. Pfeiffer, R. B. Liu, and M. S. Sherwin, Phys. Rev. X **7**, 041042 (2017).

[40] J. M. Luttinger and W. Kohn, Phys. Rev. **97**, 869 (1955).

[41] I. Vurgaftman, J. R. Meyer, and L. R. Ram-Mohan, J. Appl. Phys. **89**, 5815 (2001).

[42] M. S. Skolnick, A. K. Jain, R. A. Stradling, J. Leotin, and J. C. Ousset, J. Phys. C **9**, 2809 (1976).

[43] J. B. Costello, S. D. O'Hara, Q. Wu, M. Jang, L. N. Pfeiffer, K. W. West, and M. S. Sherwin, Phys. Rev. B **108**, 195205 (2023).

[44] S. Glutsch, U. Siegner, M.-A. Mycek, and D. S. Chemla, Phys. Rev. B **50**, 17009 (1994).